

Article

Improving the Efficiency of an Isolated Bidirectional Dual Active Bridge DC–DC Converter Using Variable Frequency

Vicente Esteve ^{1,*}, Juan L. Bellido ^{1,2}, José Jordán ¹ and Enrique J. Dede ^{1,2}

¹ Department of Electronic Engineering, University of Valencia, Av. University s/n, 46100 Burjassot, Spain; jbellido@sictechinduction.com (J.L.B.); jose.jordan@uv.es (J.J.); enrique.dede@uv.es (E.J.D.)

² R&D Department, SiCtech Induction, 46980 Paterna, Spain

* Correspondence: vesteveg@uv.es

Abstract: This article presents a control method for an isolated bidirectional dual active bridge DC–DC converter (IBDC) where single phase shift (SPS) and variable frequency (VF) modulations are combined simultaneously with the purpose of improving the efficiency of the converter applied to the bidirectional charging of electric vehicles batteries. A complete power characterization of the dual active bridge (DAB) converter is carried out. The combined control achieves lossless turn-on and turn-off on the primary bridge for a wide range of output powers. A comparative study of power losses between the traditional SPS control and the combined method proposed here was also carried out. A prototype with an output power of 10 kW was built based on Silicon Carbide (SiC) Metal Oxide Semiconductor Field-Effect Transistors (MOSFET), with which a peak efficiency close to 99% was obtained, thus verifying the viability of the method.

Keywords: power conversion; bidirectional DC–DC converter; battery energy storage; dual active bridge; single phase shift; variable frequency modulation



Citation: Esteve, V.; Bellido, J.L.; Jordán, J.; Dede, E.J. Improving the Efficiency of an Isolated Bidirectional Dual Active Bridge DC–DC Converter Using Variable Frequency. *Electronics* **2024**, *13*, 294. <https://doi.org/10.3390/electronics13020294>

Academic Editors: Tripathi Ravi Nath, Manoj Badoni, Vijay Kumar Singh and Shun-Chung Wang

Received: 11 December 2023

Revised: 1 January 2024

Accepted: 4 January 2024

Published: 9 January 2024



Copyright: © 2024 by the authors. Licensee MDPI, Basel, Switzerland. This article is an open access article distributed under the terms and conditions of the Creative Commons Attribution (CC BY) license (<https://creativecommons.org/licenses/by/4.0/>).

1. Introduction

A successful energy transition requires new strategies and careful planning to integrate all new technologies and devices for the production and storage of electrical energy. This is what some authors call “smart electrification” [1]. In this regard, electric vehicles (EVs) play a relevant role. When electric vehicles are parked and plugged-in, they can supply power to the grid or the owner’s home to meet demand peaks in what are known as vehicle-to-grid (V2G) or vehicle-to-home (V2H) strategies. Additionally, the energy stored in their batteries can help to regulate both the voltage and frequency on the grid. To achieve these capabilities, it is necessary that the converters that connect the grid with the EVs allow the bidirectional flow of energy [2].

Figure 1 shows a diagram that describes the mentioned solution for the case of a single-phase 230 V AC mains supply. The SPBR (single phase bidirectional rectifier) block is connected to the power grid through an inductance. The BDC (bidirectional DC–DC converter) block connects the EV battery to the DC link capacitor. The electronic control of the complete converter allows us to regulate the amplitude and direction of the current I_2 for the given values of the SPBR output voltage V_1 and nominal battery voltage V_2 . In a conventional battery charging process, the current I_2 flows from the network to the battery. When the battery energy is used to supply power to the grid, the direction of I_2 is the opposite [3]. It is also possible to integrate renewable energy systems and bidirectional EV chargers to facilitate smart electrification and reduce net operating costs by providing grid support and using the EV battery as a power reserve [4].

The typical topology for the SPBR block consists of a conventional transistorized single-phase full bridge boost rectifier with a pulse width modulation controlled by the input current and output voltage operating at a unity power factor and with power reversal

capability [5,6]. For three-phase mains, the preferred solution adopted is based on full bridges of three transistor legs [7,8].

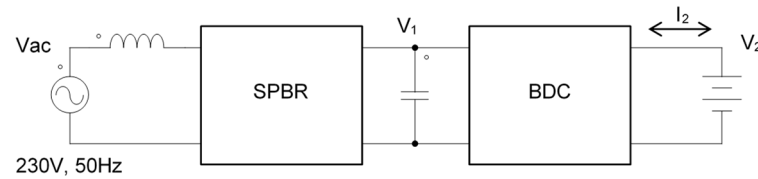


Figure 1. Block diagram of a V2G(H) converter.

The most immediate solution for the BDC consists of a simple bidirectional DC/DC converter [9], but for safety reasons, this converter must have galvanic isolation; these are the isolated bidirectional DC-DC converters (IBDC). The most accepted solution is a converter that uses two full bridges of transistors (dual active bridges—DABs) [10] or two half-bridges (dual active half-bridges—DAHBs) [11] connected so that the output of one is the input of the other. For large power levels, this topology can be optimized by using multiphase DABs [12]. One way to improve efficiency and electromagnetic interference (EMI) emission is the use of resonant DABs [13] or by means of broadband devices such as silicon carbide (SiC) [14] and gallium nitride (GaN) [15].

In DABs, the control and direction of the flow of the transferred power is carried out by shifting the operation of each of the bridges through different control techniques: single phase shift SPS [16], extended phase shift EPS [17], dual phase shift DPS [18] and triple phase shift TPS [19]. All of them are modifications of the SPS method to improve the transmission power capacity and the efficiency of the converter maintaining the zero voltage switch (ZVS) condition and minimizing the circulating current.

To achieve further improvements, hybrid control techniques are used where the DAB is controlled by phase shifting and variable frequency modulations, in sequential or independent mode, to extend the operating range of the converter while maintaining ZVS conditions [20,21] or introducing a circulating current suppression control (CCSC) that affects the DAB power transfer [22]. Ref. [23] proposes the use of a variable frequency control strategy plus an additional control loop to find the point of maximum efficiency for medium frequency (25 kHz). Other authors use variable frequency in a series resonant dual active bridge (SR-DAB) [24] or combining it with triple phase shift (VF-TPS) [25]. In order to further develop the study of these hybrid control techniques, this paper describes a variable frequency non-resonant isolated bidirectional DAB DC-DC converter (VF-IBDC) based on SiC MOSFET transistors operating at high frequency that combines SPS and VF modulations simultaneously so that the switching processes are carried out at zero voltage and also at zero current switching (ZCS) conditions in a wide operating range. In this way, high efficiency peaks, close to 99%, can be obtained with moderate EMI.

The paper is structured as follows: Section 2 focuses on the configuration of the proposed IBDC converter. In Section 3, an analysis of the conventional SPS-IBDC converter is conducted, followed by the analysis and design considerations for the proposed modulation in Section 4. Section 5 presents the comparative analysis of power losses and efficiency of the converters. In Section 6, the proposed VF-IBDC control method is introduced. The validation of results using experimental data is presented in Section 7. Finally, the conclusions are drawn.

2. IBDC Configuration

Figure 2 shows the simplified schematic of the DAB-IBDC converter which consists of two full bridges with active switches in the primary and the secondary sides, connected via the high-frequency transformer T that provides the required galvanic isolation and voltage matching between two voltage levels V_1 and V_2 . The inductor L , which also includes the leakage inductance of the transformer, serves as the instantaneous energy storage device. The duty ratio of the switching signal is 50%, but there is a phase shift

ϕ between primary and secondary bridges that defines the amplitude and direction of the power flow. C1 is the DC link capacitor connected to the output voltage V_1 of the SPBR and C2 is the output capacitor of the DAB-IBDC. In this point of voltage V_2 , the EV battery is connected. In charge mode, the power flows from C1 to C2. When the battery supplies power to the grid (discharge mode), the power flows in the opposite direction. All transistors are SiC MOSFET.

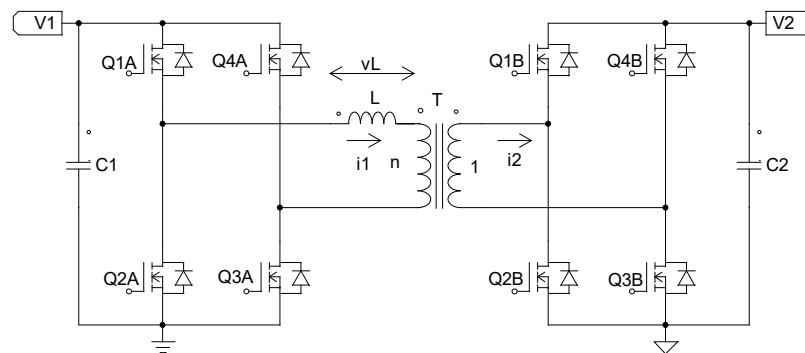


Figure 2. DAB-IBDC configuration.

The design has been made for a fast bidirectional charging application of lithium-ion EV batteries using a typical conventional charging process [26]. Table 1 shows several values that serve as specifications for the converter design. When the converter delivers maximum power in the first phase of the charging process, the output current must be regulated independently of the existing battery voltage.

Table 1. DAB-IBDC specifications.

Specification	Symbol	Value	Unit
Maximum Power	P_{max}	10	kW
Initial Switching Frequency	f	100	kHz
Regulated DC Input Voltage	V_1	385	V
Minimum DC Output Voltage	$V_2 min$	285	V
Maximum DC Output Voltage	$V_2 max$	400	V
Maximum Output Current	I_2	25	A

3. Analysis of the SPS-IBDC

Figure 3 shows the main simplified waveforms of the SPS-IBDC in charge mode (top) and discharge mode (bottom). The black waveforms are the switching signals of transistor Q1A and Q3A in the primary bridge, and Q1B and Q3B in the secondary bridge. The switching signals of Q2A and Q4A, and Q2B and Q4B are delayed by 180° . All of these signals are shown as square signals (with duty cycle $D = 0.5$) because dead time was not considered to simplify the graph. The blue waveforms represent the voltage across the inductance L, the red waveforms show the output current of the primary bridge, and the green waveforms are the input current of the secondary bridge. Note that the sign of ϕ determines the mode of operation so that if ϕ is positive, the converter acts in charge mode, and if ϕ is negative, it acts in discharge mode.

To extract properties and be able to design the circuit, it is necessary to carry out a complete analysis to obtain the equations that describe the behavior of its voltages and currents. The aim is to obtain a single set of equations that can describe the circuit in charging or discharging operating mode at the same time. The observation of the similarities and differences of the voltage waveforms in the inductance allows us to define two new parameters, δ and V_2^* , given by

$$\delta = \begin{cases} \varphi & \text{if } \varphi \geq 0 \\ \varphi + \pi & \text{if } \varphi < 0 \end{cases} \quad (1)$$

$$V_2^* = \begin{cases} V_2 & \text{if } \varphi \geq 0 \\ -V_2 & \text{if } \varphi < 0. \end{cases} \quad (2)$$

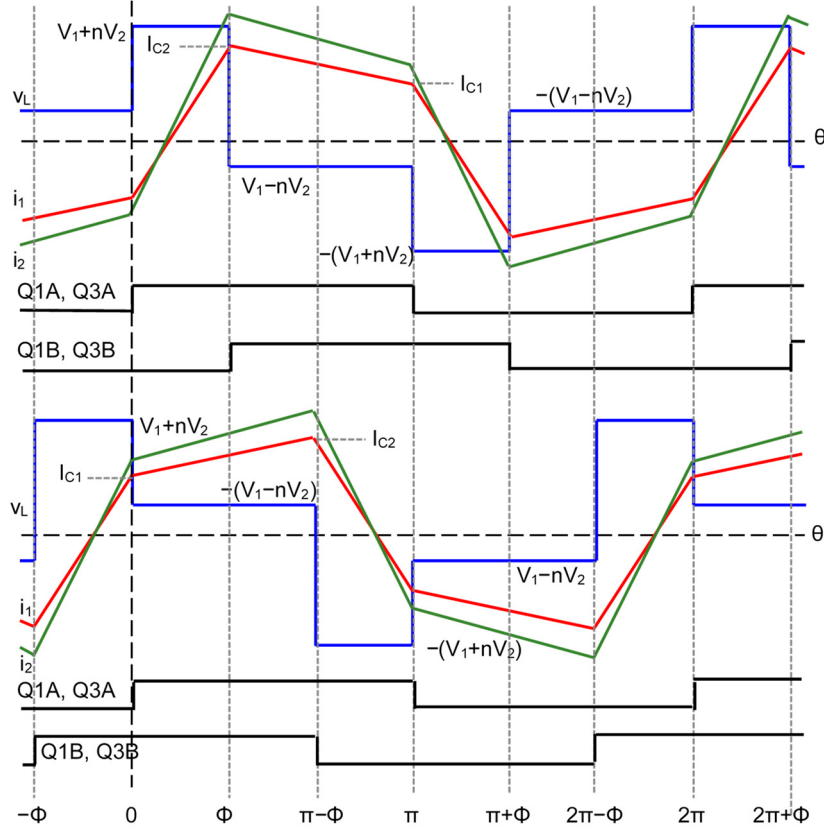


Figure 3. Simplified voltage and current waveforms of SPS-IBDC.

After this, the voltage $v_L(\theta)$ of the inductance and the output current of the primary bridge $i_1(\theta)$ for any operating cycle can be determined by means of next piecewise equations:

$$v_L(\theta) = \begin{cases} V_1 + nV_2^* & \text{if } 0 \leq \theta < \delta \\ V_1 - nV_2^* & \text{if } \delta \leq \theta < \pi \\ -(V_1 + nV_2^*) & \text{if } \pi \leq \theta < \pi + \delta \\ -(V_1 - nV_2^*) & \text{if } \pi + \delta \leq \theta < 2\pi \end{cases} \quad (3)$$

$$i_1(\theta) = \begin{cases} \frac{V_1+nV_2^*}{L\omega}\theta + \frac{nV_2^*(\pi-2\delta)-\pi V_1}{2L\omega} & \text{if } 0 \leq \theta < \delta \\ \frac{V_1-nV_2^*}{L\omega}\theta + \frac{nV_2^*(\pi+2\delta)-\pi V_1}{2L\omega} & \text{if } \delta \leq \theta < \pi \\ -\frac{V_1+nV_2^*}{L\omega}\theta + \frac{nV_2^*(\pi+2\delta)+3\pi V_1}{2L\omega} & \text{if } \pi \leq \theta < \pi + \delta \\ -\frac{V_1-nV_2^*}{L\omega}\theta + \frac{nV_2^*(-3\pi-2\delta)+3\pi V_1}{2L\omega} & \text{if } \pi + \delta \leq \theta < 2\pi \end{cases} \quad (4)$$

with $\omega = 2\pi f$ where f is the switching frequency. Integrating the square of (3) and (4), it is possible to calculate the corresponding root mean square (rms) values:

$$V_{1rms} = \frac{1}{\pi} \sqrt{\delta(nV_1 + V_2)^2 + (\pi - \delta)(V_2 - nV_1)^2} \quad (5)$$

$$I_{1rms} = \frac{\pi}{2\sqrt{3}L\omega} \sqrt{V_1^2 + 2nV_1V_2 \left(-4\frac{\delta^3}{\pi^3} + 6\frac{\delta^2}{\pi^2} - 1 \right) + n^2V_2^2} \quad (6)$$

and the values of the switching currents can be obtained:

$$I_{C1} = \frac{\pi V_1 - nV_2(\pi - 2\delta)}{2L\omega} \quad (7)$$

$$I_{C2} = \frac{n\pi V_2 - V_1(\pi - 2\delta)}{2L\omega}. \quad (8)$$

The value of the active power transferred between the primary and the secondary bridges can be obtained by calculating the average value of the instantaneous product of the voltage and the current in the transformer given by:

$$P = \frac{nV_1 V_2 \delta (\delta - \pi)}{\pi L \omega}. \quad (9)$$

When the phase shift ϕ is 90° , the maximum value of the power is transferred, which is

$$P_{\max} = \frac{n\pi V_1 V_2}{4L\omega}. \quad (10)$$

Figure 4 shows the evolution of the transferred power in units normalized to the maximum power value given in (10) as a function of the phase ϕ for the minimum and maximum values of the voltage V_2 of the battery. The power transferred during the charging or discharging process at maximum output current (positive or negative) should remain between the two curves.

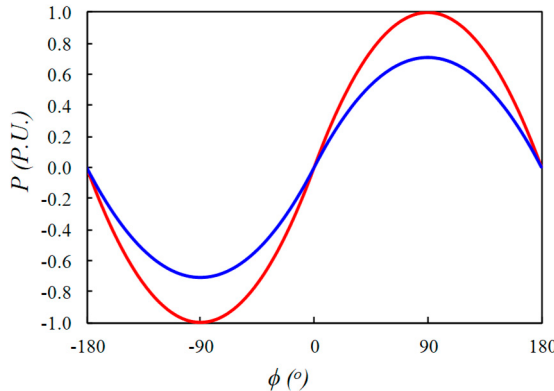


Figure 4. Transferred power of the SPS-IBDC versus phase shift. The red line corresponds to $V_2 = 400$ V, and the blue line corresponds to $V_2 = 285$ V.

From (10), the equation that allows the design of the inductance L can be obtained,

$$L = \frac{nV_1 V_2}{8P_{\max} f}. \quad (11)$$

To improve the efficiency and reduce the EMI of the converter, it is necessary that the switching of the transistors be carried out in ZVS mode. This is only possible when (4) is positive, which determines a minimum value for the phase given by

$$\delta_{\min} = \frac{\pi (nV_2 - V_1)}{2nV_2}; \quad (12)$$

therefore, the range where ZVS is possible is

$$\delta_{\min} < |\varphi| \leq \pi/2. \quad (13)$$

Substituting (12) into (9), we got

$$P_{\min} = \frac{V_1(n^2 V_2^2 - V_1^2)}{8nLV_2f} \quad (14)$$

then, the power range in ZVS mode is determined by

$$P_{\min} < |P| \leq P_{\max}. \quad (15)$$

4. Analysis of the VF-IBDC

In the previous section, conditions were found to keep the primary (or secondary) bridge working in ZVS mode, and it is only possible to obtain ZCS switching for the δ_{\min} phase where the waveforms become those shown in Figure 5.

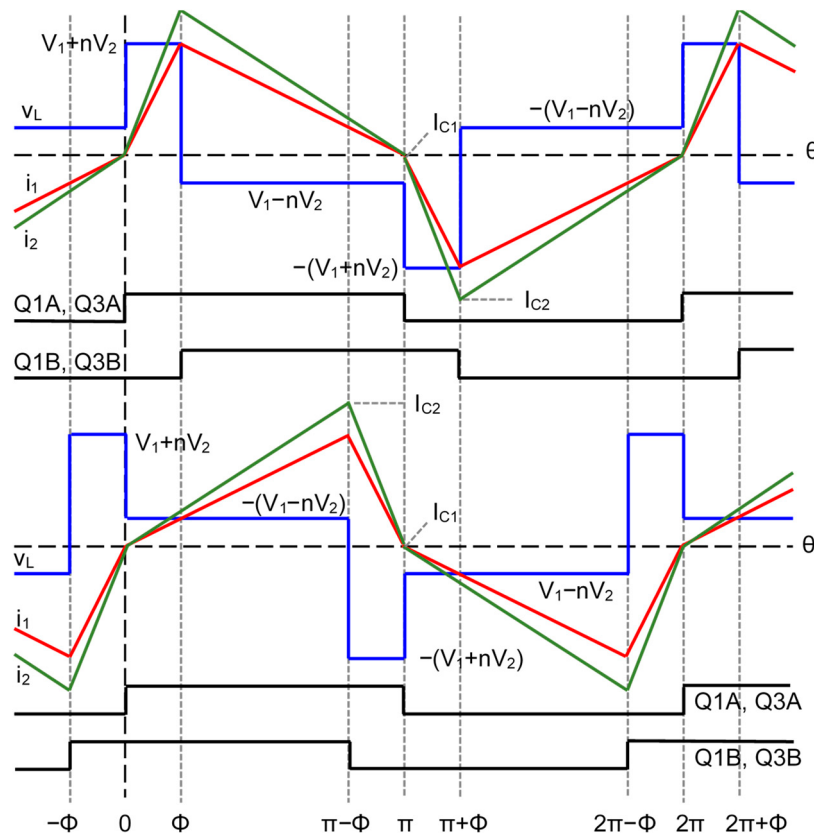


Figure 5. Simplified voltage and current waveforms of VF-IBDC.

The signals in Figure 5 are the same as those in Figure 3, also showing the waveforms in charge mode (top) and discharge mode (bottom). Note that both turn-on and turn-off switching are carried out near the zero crossing of the current. This is an ideal situation where switching losses are minimal. To extend this condition with other power values, we should modify the switching frequency while maintaining the ZVS-ZCS condition with the appropriate adjustment of the phase so that δ meets (12). Therefore, the power is determined by (14) varying the phase shift and the switching frequency simultaneously. This is the concept of hybrid control that we present in the first section of this paper.

To carry out the converter design, the allowed frequency variation range must initially be set. Extending the frequency to very high values would increase the switching losses of the semiconductors and cause excessive conductor losses due to the skin effect, while frequencies that are too low would raise the flux density of the transformer and inductor core, increasing its losses or even causing magnetic saturation. In the present design, the allowed range goes from 100 kHz to 400 kHz for the highest possible range of transferred power.

If the output current I_2 is maintained at its maximum value for any value of battery voltage between V_{2min} and V_{2max} , the following design equation can be obtained to determine the value of the ratio transformer n :

$$n = \frac{V_1}{V_{2max} V_{2min}} \sqrt{\frac{k V_{2max}^2 - V_{2min}^2}{k - 1}} \quad (16)$$

where $k = f_1/f_2$. Since (14) shows that power is inversely proportional to frequency, values for f_1 and f_2 are chosen in the lower part of the determined range. Given $f_1 = 100$ kHz and $f_2 = 200$ kHz, $n = 1.65$ is obtained.

Now, (11) is not valid and the value of L is obtained by isolating it from (14),

$$L = \frac{V_1 (n^2 V_{2max}^2 - V_1^2)}{8n P_{max} V_{2max} f}. \quad (17)$$

Taking into account the values in Table 1 and the value of n in (16), a value of $L = 10.48 \mu\text{H}$ is obtained.

Figure 6 shows the evolution of the absolute value of transferred power in normalized units in function of the switching frequency for the minimum and maximum values of the voltage V_2 of the battery. The power transferred at maximum output current in ZVS and ZCS condition should remain between the two curves.

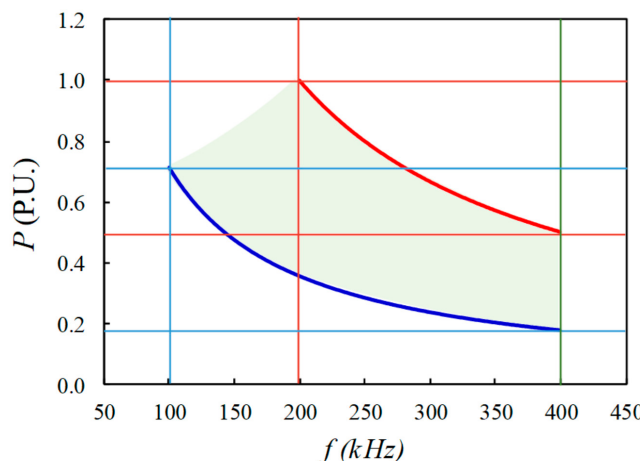


Figure 6. Transferred power of the VF-IBDF converter versus switching frequency. The red line corresponds to $V_2 = 400$ V, and the blue line corresponds to $V_2 = 285$ V.

5. Comparative Analysis of Power Losses and Efficiency

A power loss analysis of the SPS-IBDC and VF-IBDC has been carried out considering the contribution of conduction and switching losses of the transistors, and the power losses of the core and the windings of the inductor and the transformer. In this study, residual losses in other non-active components (capacitors, cables, etc.) have not been considered. The analysis of P_{sw} focuses solely on the turn-off losses of the inverter bridge transistors as the turn-on switching losses are negligible due to the ZVS condition [27].

In the practical implementation of the converter, the primary and secondary bridge switches have been configured differently. The primary bridge is made up of four switches with a single transistor; however, as the secondary bridge has more losses, each of its switches has two transistors in parallel. The transistor chosen is the SiC MOSFET C3M0016120K of $V_{DS} = 1200$ V and $R_{Dson} = 16 \text{ m}\Omega$.

The losses in the diodes have been neglected since the conduction of the reverse current is also carried out through the transistor channel except during dead times. Thus, conduction losses for each transistor can be calculated only using (18).

$$P_{CD1} = \left(\frac{I_{1rms}}{\sqrt{2}} \right)^2 R_{DSon} \quad (18)$$

$$P_{CD2} = \left(\frac{nI_{1rms}}{2\sqrt{2}} \right)^2 R_{DSon} \quad (19)$$

where P_{CD1} represents the conduction power losses of the primary bridge and P_{CD2} represents the conduction power losses of secondary bridge.

The switching power losses of each transistor of the primary and secondary bridges can be calculated using the graphs of the turn-off switching energy E_{off} provided by the manufacturer using the following polynomial function.

$$E_{off1} = a I_{C1}^2 + b I_{C1} + c \quad (20)$$

$$E_{off2} = a \left(\frac{nI_{C2}}{2} \right)^2 + b \frac{nI_{C2}}{2} + c \quad (21)$$

where a , b and c take the following values:

$$a = 0.048 \text{ } \mu\text{J A}^{-1/2}$$

$$b = 1.064 \text{ } \mu\text{J A}^{-1}$$

$$c = 10 \text{ } \mu\text{J}$$

The switching turn-off losses of each transistor can be calculated with

$$P_{SW1} = E_{off1} f \quad (22)$$

$$P_{SW2} = E_{off2} f. \quad (23)$$

On the other hand, the core losses of the inductor can be obtained using next equation:

$$P_{II} = P_{DI} V_{II} \quad (24)$$

where P_{DI} is the core loss density of the inductor given by the manufacturer for the operating frequency and magnetic flux density, and V_{II} is its volume. The inductor core is composed of two pieces of KOOL MU 6527 U core from Magnetics.

Analogously, the losses of the transformer core can be obtained by

$$P_{TI} = P_{DT} V_{TI} \quad (25)$$

where P_{DT} is the core loss density of the transformer, and V_{TI} is its volume. The transformer core is made with two pieces of the uncoated ferrite core U 126/91/20 from Magnetics. In both cases, the designs have been made with a flux density that guarantees non-saturation of the magnetic material. Specifically, the maximum flux density in the inductor core is 190 mT, and it is 100 mT in the transformer core.

In order to calculate the copper losses P_{IC} of the inductor, it is necessary to know the effective resistance of the winding R_I taking into account the conductivity, the total length and the skin effect using

$$P_{IC} = I_{Irms}^2 R_I. \quad (26)$$

For the two windings of the transformer, the power loss P_{TC} is given by

$$P_{TC} = I_{Irms}^2 (R_{T1} + n^2 R_{T2}) \quad (27)$$

where R_{T1} and R_{T2} are the effective resistance of the primary and secondary transformer windings, respectively.

Therefore, the total power loss of the converter is

$$P_{tot} = 4(P_{CD1} + P_{SW1}) + 8(P_{CD2} + P_{SW2}) + P_{II} + P_{TI} + P_{IC} + P_{TC} \quad (28)$$

and the efficiency of the inverter can be calculated using

$$\eta = \frac{P_o}{P_o + P_{tot}} \quad (29)$$

Table 2 shows the calculated results of the power loss analysis for the VF-IBDC converter specified in Table 1 operating at maximum output current.

Table 2. Power loss analysis of VF-IBDC.

Magnitude	Symbol	$V_2 = 400$ V	$V_2 = 285$ V	Unit
Primary bridge transistor conduction losses	P_{CD1}	7.2	3.6	W
Second. Bridge transistor conduction losses	P_{CD2}	4.9	2.5	W
Primary bridge transistor switching losses	P_{SW1}	2.0	1.0	W
Second. Bridge transistor switching losses	P_{SW2}	28.7	8.7	W
Total primary bridge losses	$4(P_{CD1} + P_{SW1})$	36.8	18.6	W
Total secondary bridge losses	$8(P_{CD2} + P_{SW2})$	269.1	89.6	W
Total inductor core losses	$P_{II} + P_{IC}$	18.6	2.6	W
Total transformer losses	$P_{TI} + P_{TC}$	74.6	10.4	W
Efficiency	η	96.2	98.3	%

Figure 7 shows the evolution of the power losses and the efficiency of the VF-IBDC converter for different values of the output power expressed in normalized units referring to the value of the maximum output power. When the battery has its minimum voltage value (285 V), the loss and efficiency curves are shown in blue, while for the maximum voltage value (400 V), the curves are red. As the maximum charging current is the same in both cases (25 A), the maximum power obtained is reduced from 10,000 W to 7125 W when the battery voltage goes from 400 V to 285 V.

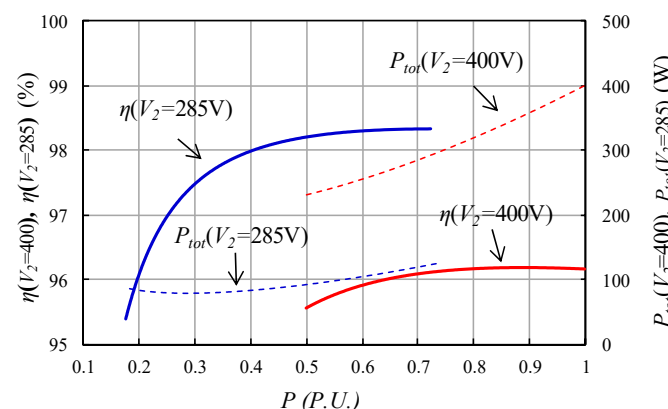


Figure 7. VF-IBDC's total power losses (dashed line) and efficiency (solid line) in front of output power for $V_2 = 400$ V (red) and $V_2 = 285$ V (blue).

Table 3 shows the calculated results of the power loss analysis for the SPS-IBDC working in the same conditions maintaining the transformer configurations and changing the value of $L = 15.88 \mu\text{H}$ in order to obtain the maximum power determined in (11).

Table 3. Power loss analysis of SPS-IBDC.

Magnitude	Symbol	$V_2 = 400 \text{ V}$	$V_2 = 285 \text{ V}$	Unit
Primary bridge transistor conduction losses	P_{CD1}	9.7	6.2	W
Second. bridge transistor conduction losses	P_{CD2}	6.6	4.2	W
Primary bridge transistor switching losses	P_{SW1}	17.4	17.4	W
Secondary bridge transistor switching losses	P_{SW2}	29.0	17.6	W
Total primary bridge losses	$4(P_{CD1} + P_{SW1})$	108.5	94.2	W
Total secondary bridge losses	$8(P_{CD2} + P_{SW2})$	284.9	174.2	W
Total inductor losses	$P_{II} + P_{IC}$	18.9	9.6	W
Total transformer losses	$P_{TI} + P_{TC}$	75.8	38.5	W
Efficiency	η	95.4	95.8	%

To complete the comparative loss analysis, Figure 8 shows the power losses and efficiency of the SPS-IBDC converter versus output power.

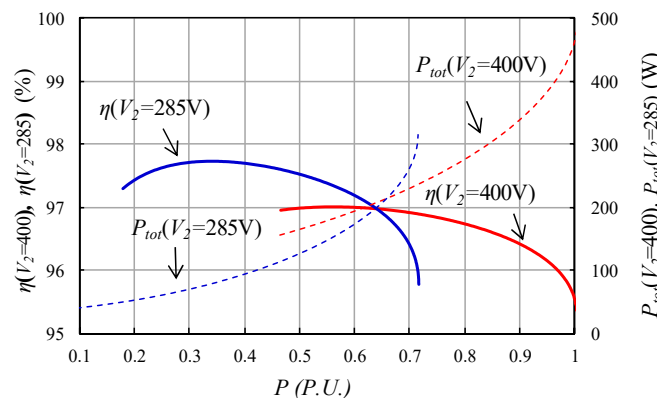


Figure 8. SPS-IBDC total power losses (dashed line) and efficiency (solid line) in front of output power for $V_2 = 400 \text{ V}$ (red) and $V_2 = 285 \text{ V}$ (blue).

Comparing Tables 2 and 3, it is observed that the VF-IBDC presents an efficiency improvement of 6 percentage points at minimum battery voltage and maximum charging current. Looking at Figures 7 and 8, a general improvement in efficiency is also observed at high output power values.

6. VF-IBDC Control Schema

The control circuit designed to implement the VF-IBDC is an adaptive variable frequency and phase shift system that must be able to perform ZVS and quasi-ZCS in the primary bridge under wide operating conditions. Figure 9 shows the block diagram of the proposed control circuit.

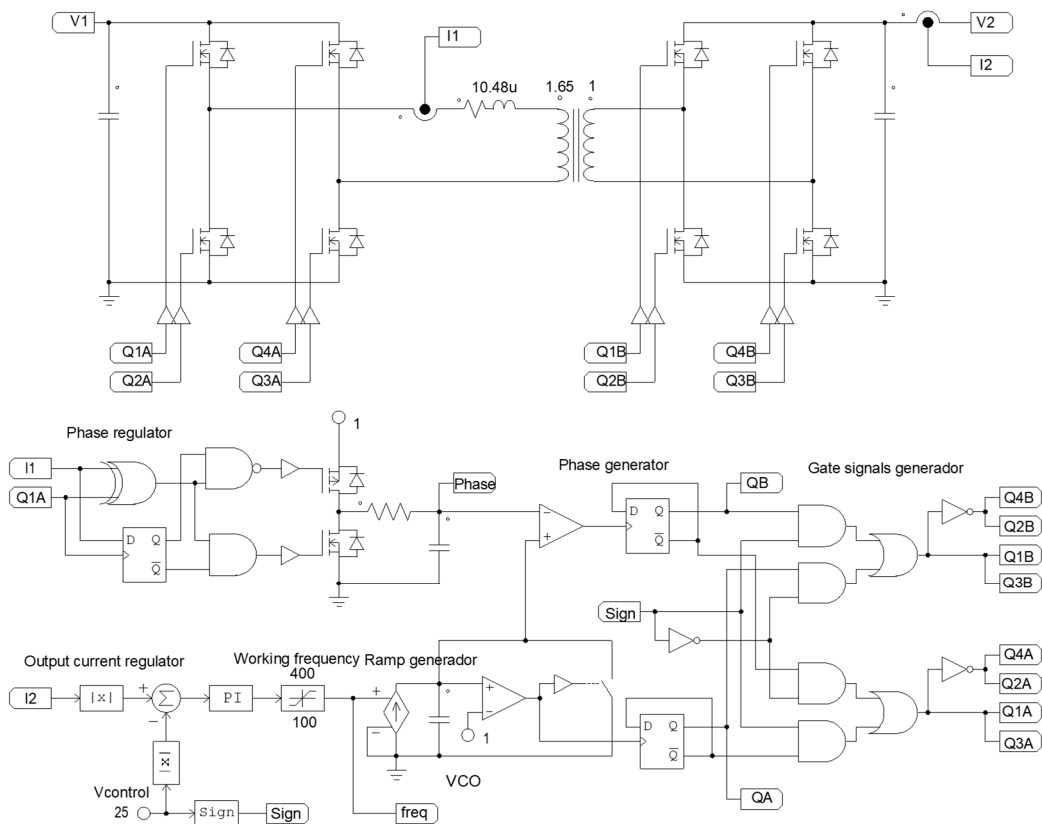


Figure 9. Block diagram of the proposed control circuit.

The main variable to control is the battery charging current I_2 , taking into account that its sign is defined as positive when the converter is in charge mode and negative when it acts in discharge mode. Since the phase detector and the VCO act like a phase-locked loop, the signal Q_{1A} will be in phase with the primary bridge output current I_1 to guarantee the ZVS-ZCS primary bridge operation. The output current I_2 is regulated with the PI controller, keeping its absolute value equal to the reference value $V_{control}$, obtaining the values of switching frequency that enters the VCO. The sign block detects the sign of the current reference and controls the gate signals generator to manage the power transfer direction. Other secondary loops not shown in this diagram would limit the values of V_1 , I_1 and V_2 during the power transfer process.

7. Experimental Results

This section shows the experimental results obtained by testing a 10 kW VF-IBDC converter operating according to the specifications shown in Table 1. The values of the components of the circuit are those obtained in previous sections. For the experimental verification, a test bed was constructed, consisting of the following elements:

- A primary bridge with four C3M0016120K SiC MOSFETs mounted on a water cooling heatsink.
- A secondary bridge with eight C3M0016120K SiC MOSFETs mounted on a water cooling heatsink.
- An inductor L of $10.5 \mu\text{H}$ (including transformer leakage inductance).
- A transformer T with $n = 10:6$.
- An integrated digital electronic control on an FPGA-based system.

A and B are fully functional full bridge modules that include sensors, transistor trigger circuits and a power supply with galvanic isolation and high common-mode transient immunity (CMTI). V_1 and V_2 have been realized through IT6012C-800-50 bidirectional

laboratory power supplies. Figure 10 shows a picture of the test bed used to obtain the following experimental results.

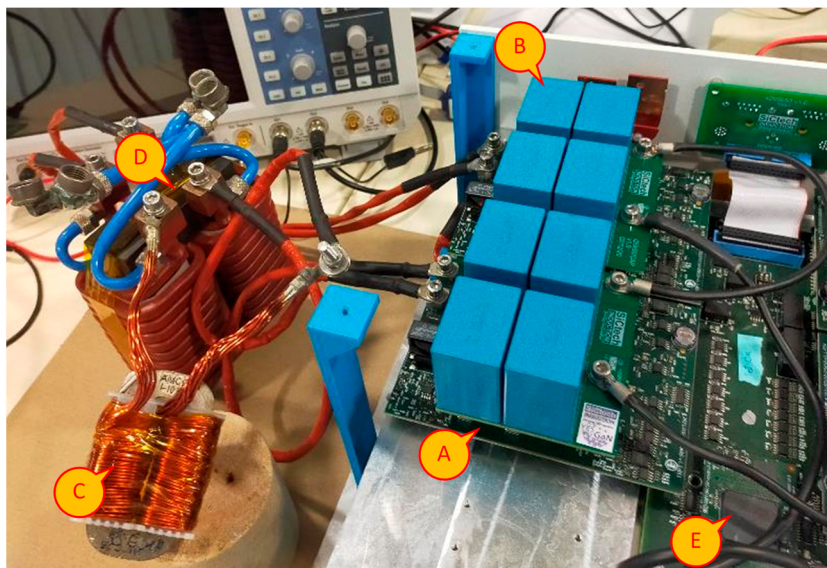


Figure 10. Test bed.

Figure 11 displays waveforms captured by a digital oscilloscope for the VF-IBDC converter operating at full power in charge mode with 385 V at the input. In Figure 11a, the output voltage is 400 V, and in Figure 11b, the output voltage is 285 V. In order to keep ZVS and quasi-ZCS conditions, the frequency changes from 197 kHz ($V_2 = 400$ V) to 98 kHz ($V_2 = 285$ V). The control circuit regulates the output current of 25 A constant in both cases.

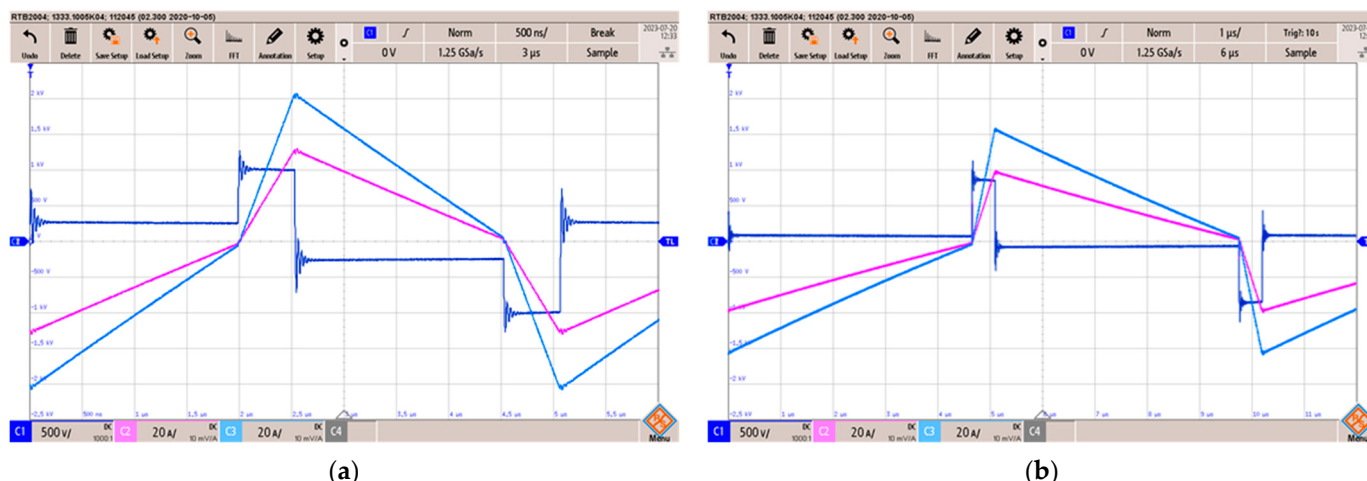


Figure 11. Experimental waveforms of the VF-IBDC in charge mode with $V_1 = 385$ V and $V_2 = 400$ V (a) when $P = 10$ kW and (b) when $P = 7125$ W. C1 (dark blue) is the inductor voltage (500 V/div), C2 (magenta) is the primary bridge output current (20 A/div), and C3 (light blue) is the secondary bridge input current (20 A/div). Time base is 0.5 μ s/div.

Figure 12 shows oscillograms in discharge mode when the power goes from $V_2 = 400$ V in Figure 12a or $V_2 = 285$ V in Figure 12b with $V_1 = 385$ V. Now, the regulated current I_2 is -25 A. The change of frequency in discharge mode is quite similar to that in charge mode.

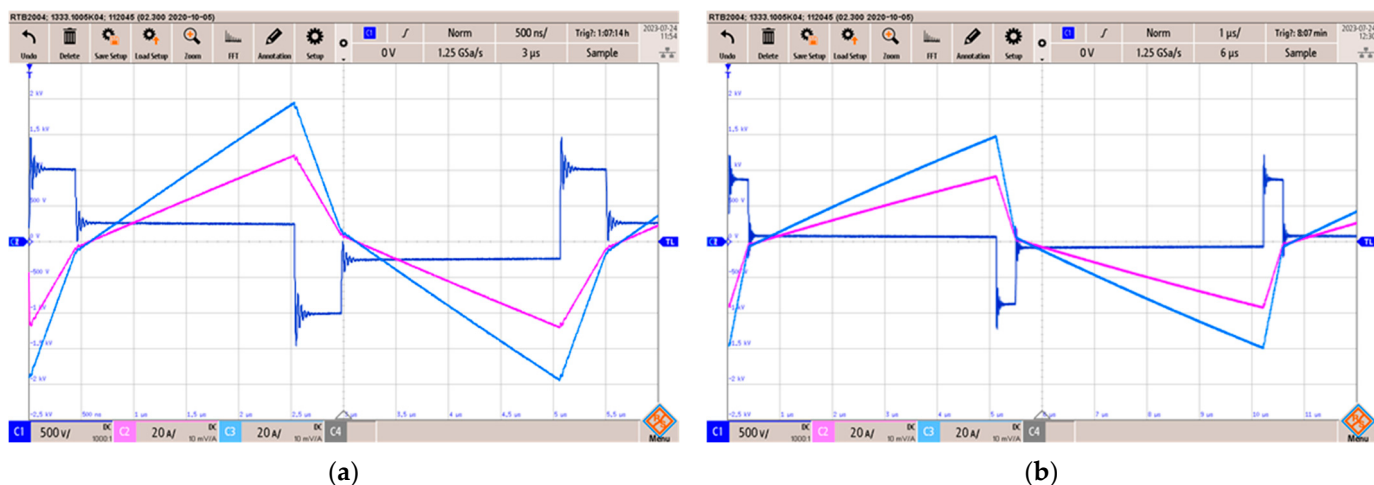


Figure 12. Experimental waveforms of the VF-IBDC in discharge mode with $V_1 = 385$ V and $V_2 = 400$ V (a) when $P = 10$ kW and (b) when $P = 7125$ W. C1 (dark blue) is the inductor voltage (500 V/div), C2 (magenta) is the primary bridge output current (20 A/div) and C3 (light blue) is the secondary bridge input current (20 A/div). Time base is 0.5 μ s/div.

Finally, Figure 13 shows the experimental measurements of the efficiency in charge mode regulating the output current until 25 A with $V_1 = 385$ V when V_2 is 400 V (red lines) and 285 V (blue lines). The results obtained in discharge mode were very similar. Note that there are some differences between the experimental and calculated results that may be due to the modeling method used, the existence of losses of other elements not taken into account in the calculation (capacitors, conductors, parasitic components, voltage and current sensors, etc.) and also the measurement process.

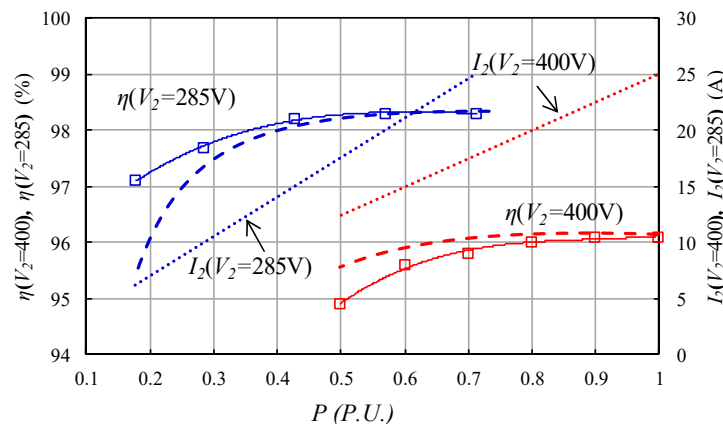


Figure 13. Calculated and experimental efficiency of VF-IBDC converter in function of normalized output power. Solid lines and marking symbols represent the experimental measurements. Dashed lines represent theoretical predictions. Dotted lines represent the evolution of the current I_2 during the tests.

8. Discussion and Conclusions

This paper has carried out a complete study of the VF-IBDC converter that explores the combined effect of a variable frequency and a phase shift to control an isolated bidirectional dual active bridge DC–DC converter so that its primary bridge operates under ZVS and quasi-ZCS conditions over a wide operating range.

After an in-depth analysis of the operation of the SPS-IBDC, a complete design procedure has been presented that allows for the design of a VF-IBDC converter for a specific application of bidirectional charging of electric vehicle batteries.

To verify the viability of the design, a comparative analysis of power losses was developed that determined that the VF-IBDC converter is an enhanced solution that allows us to improve efficiency by up to 6 percentage points compared to the standard SPS method.

A fully functional control circuit has also been presented, easily implementable on the PSIM simulator, which allows us to check the correct operation of the converter and which was the basis of the control finally implemented on an FPGA-based system.

The feasibility of this design has been verified with the construction and testing of a 10 kW converter using SiC MOSFET transistors where an efficiency greater than 98% was achieved.

Author Contributions: Conceptualization and methodology, V.E.; software, J.L.B.; validation, J.J.; formal analysis, V.E.; resources, E.J.D.; data curation, J.L.B.; writing, editing and visualization, V.E. and J.L.B.; supervision, V.E.; project administration and funding acquisition, E.J.D. All authors have read and agreed to the published version of the manuscript.

Funding: This work has been carried out in the framework of the European Project “YESvGaN”. The project has received funding from the Electronic Component Systems for European Leadership Joint Undertaking (ECSEL JU), under grant agreement No. 101007229. This Joint Undertaking receives support from the European Union’s Horizon 2020 Research and Innovation Programme, and Germany, France, Belgium, Austria, Sweden, Spain, and Italy.

Data Availability Statement: The data presented in this study are available on request from the corresponding author. The data are not publicly available due to privacy restrictions.

Conflicts of Interest: Authors Juan L. Bellido and Enrique J. Dede were employed by the company SiCtech Induction. The remaining authors declare that the research was conducted in the absence of any commercial or financial relationships that could be construed as a potential conflict of interest.

References

- IRENA. *Smart Electrification with Renewables: Driving the Transformation of Energy Services*; International Renewable Energy Agency: Abu Dhabi, Saudi Arabia, 2022.
- Zhou, K.; Fang, H.; Liu, Y. Driving–Charging Integrated Controller for Electric Vehicles. *IEEE Access* **2022**, *10*, 66545–66563. [[CrossRef](#)]
- Monteiro, V.; Pinto, J.G.; Afonso, J.L. Operation Modes for the Electric Vehicle in Smart Grids and Smart Homes: Present and Proposed Modes. *IEEE Trans. Veh. Technol.* **2016**, *65*, 1007–1020. [[CrossRef](#)]
- Bassa de los Mozos, A.; Chandra Mouli, G.R.; Bauer, P. Evaluation of topologies for a solar powered bidirectional electric vehicle charger. *IET Power Electron.* **2019**, *12*, 3675–3687. [[CrossRef](#)]
- Kim, H.-S.; Ryu, M.-H.; Baek, J.-W.; Jung, J.-H. High-Efficiency Isolated Bidirectional AC–DC Converter for a DC Distribution System. *IEEE Trans. Power Electron.* **2012**, *28*, 1642–1654. [[CrossRef](#)]
- Singh, B.; Singh, B.N.; Chandra, A.; Al-Haddad, K.; Pandey, A.; Kothari, D.P. A review of single -phase improved power quality AC–DC converters. *IEEE Trans. Ind. Electron.* **2003**, *50*, 962–981. [[CrossRef](#)]
- Kolar, J.W.; Friedli, T. The essence of three-phase PFC rectifier systems—Part I. *IEEE Trans. Power Electron.* **2013**, *28*, 176–198. [[CrossRef](#)]
- Schrittwieser, L.; Kolar, J.W.; Soeiro, T.B. Novel SWISS Rectifier Modulation Scheme Preventing Input Current Distortions at Sector Boundaries. *IEEE Trans. Power Electron.* **2017**, *32*, 5771–5785. [[CrossRef](#)]
- Jahnes, M.; Zhou, L.; Eull, M.; Wang, W.; Preindl, M. Design of a 22-kW Transformerless EV Charger with V2G Capabilities and Peak 99.5% Efficiency. *IEEE Trans. Ind. Electron.* **2023**, *70*, 5862–5871. [[CrossRef](#)]
- Inoue, S.; Akagi, H. A bidirectional dc–dc converter for an energy storage system with galvanic isolation. *IEEE Trans. Power Electron.* **2007**, *22*, 2299–2306. [[CrossRef](#)]
- Inoue, S.; Ishigaki, M.; Takahashi, A.; Sugiyama, T. Design of an Isolated Bidirectional DC–DC Converter with Built-in Filters for High Power Density. *IEEE Trans. Power Electron.* **2021**, *36*, 739–750. [[CrossRef](#)]
- De Doncker, R.W.; Divan, D.M.; Kheraluwala, M.H. A three-phase soft-switched high-power-density DC/DC converter for high-power applications. *IEEE Trans. Ind. Appl.* **1991**, *27*, 63–73. [[CrossRef](#)]
- Mi, C.; Wang, C.; Gargies, S. Operation, design and control of dual H-bridge-based isolated bidirectional dc–dc converter. *IET Power Electron.* **2008**, *1*, 507–517. [[CrossRef](#)]
- Lee, B.-K.; Kim, J.-P.; Kim, S.-G.; Lee, J.-Y. An Isolated/Bidirectional PWM Resonant Converter for V2G(H) EV On-Board Charger. *IEEE Trans. Veh. Technol.* **2017**, *66*, 7741–7750. [[CrossRef](#)]
- Biela, J.; Schweizer, M.; Waffler, S.; Kolar, W. SiC versus Si Evaluation of potentials for performance improvement of inverter and dc–dc converter systems by SiC power semiconductors. *IEEE Trans. Ind. Electron.* **2011**, *58*, 2872–2882. [[CrossRef](#)]

16. Zhang, Z.; Huang, J.; Xiao, Y. GaN-Based 1-MHz Partial Parallel Dual Active Bridge Converter with Integrated Magnetics. *IEEE Trans. Ind. Electron.* **2021**, *68*, 6729–6738. [[CrossRef](#)]
17. Zhao, B.; Yu, Q.; Sun, W. Extended-phase-shift control of isolated bidirectional dc-dc converter for power distribution in microgrid. *IEEE Trans. Power Electron.* **2012**, *27*, 4667–4680. [[CrossRef](#)]
18. Zhao, B.; Song, Q.; Liu, W. Power characterization of isolated bidirectional dual-active-bridge dc-dc converter with dual-phase-shift control. *IEEE Trans. Power Electron.* **2012**, *27*, 4172–4176. [[CrossRef](#)]
19. Krismer, F.; Kolar, J.W. Efficiency-optimized high-current dual active bridge converter for automotive applications. *IEEE Trans. Ind. Electron.* **2012**, *59*, 2745–2760. [[CrossRef](#)]
20. Chan, H.L.; Cheng, K.W.E.; Sutanto, D. ZCS-ZVS bidirectional phase-shifted dc-dc converter with extended load range. *IEE Proc. Electr. Power Appl.* **2003**, *150*, 269–277. [[CrossRef](#)]
21. Hiltunen, J.; Väisänen, V.; Juntunen, R.; Silventoinen, P. Variable-Frequency Phase Shift Modulation of a Dual Active Bridge Converter. *IEEE Trans. Power Electron.* **2015**, *30*, 7138–7148. [[CrossRef](#)]
22. Aguilar, R.; Tarisciotti, L.; Pereda, J. Circulating Current Suppression in DAB Assisted Low-Voltage Variable Frequency MMC. *IEEE Trans. Ind. Appl.* **2022**, *58*, 6322–6331. [[CrossRef](#)]
23. Erni, I.R.; Vidal-Idiarte, E.; Calvente, J.; Guasch-Pesquer, L. Small Signal Modelling for Variable Frequency Control with Maximum Efficiency Point Tracking of DAB Converter. *IEEE Access* **2021**, *9*, 85289–85299. [[CrossRef](#)]
24. Chen, T.; Yu, R.; Huang, A.Q. A Bidirectional Isolated Dual-Phase-Shift Variable-Frequency Series Resonant Dual-Active-Bridge GaN AC-DC Converter. *IEEE Trans. Ind. Electron.* **2023**, *70*, 3315–3325. [[CrossRef](#)]
25. Tang, Y.; Hu, W.; Cao, D.; Hou, N.; Li, Z.; Li, Y.W.; Chen, Z.; Blaabjerg, F. Deep Reinforcement Learning Aided Variable-Frequency Triple-Phase-Shift Control for Dual-Active-Bridge Converter. *IEEE Trans. Ind. Electron.* **2023**, *70*, 10506–10515. [[CrossRef](#)]
26. Meng, J.; Ricco, M.; Luo, G.; Swierczynski, M.; Stroe, D.-I.; Stroe, A.-I.; Teodorescu, R. An Overview and Comparison of Online Implementable SOC Estimation Methods for Lithium-Ion Battery. *IEEE Trans. Ind. Appl.* **2018**, *54*, 1583–1591. [[CrossRef](#)]
27. Esteve, V.; Jordán, J.; Dede, E.J.; Martinez, P.J.; Ferrara, K.J.; Bellido, J.L. Comparative analysis and improved design of LLC inverters for induction heating. *IET Power Electron.* **2023**, *16*, 1754–1764. [[CrossRef](#)]

Disclaimer/Publisher’s Note: The statements, opinions and data contained in all publications are solely those of the individual author(s) and contributor(s) and not of MDPI and/or the editor(s). MDPI and/or the editor(s) disclaim responsibility for any injury to people or property resulting from any ideas, methods, instructions or products referred to in the content.